JOURNAL OF SOLID STATE CHEMISTRY 2, 366–376 (1970)

Structural Studies by Electron Microscopy: Polymorphism of $ZrO_2 \cdot 12Nb_2O_5$

J. G. ALLPRESS

CSIRO, Division of Tribophysics, University of Melbourne, Parkville, Victoria 3052, Australia

AND

R. S. ROTH

Institute for Materials Research, National Bureau of Standards, Washington, D.C. 20234

Received April 7, 1970

Three polymorphs of $ZrO_2 \cdot 12Nb_2O_5$ have been identified by the combined use of X-ray diffraction and electron optical techniques. The α form, which is the initial product of the reaction of ZrO_2 with Nb_2O_5 in the molar ratio 1:12, is isostructural with $TiNb_{24}O_{62}$. The monoclinic β form, produced by long annealing, has a more complex structure, and may contain intergrowths of a third, γ, polymorph. Lattice images of the β form, together with the diffraction data, are used to derive possible structures for these materials.

1. Introduction

Several phase studies (*1*, *2*) of the system ZrO_2–Nb_2O_5 have indicated the existence of a considerable solid-solubility of ZrO_2 in Nb_2O_5. A subsequent more detailed examination of this region of the phase diagram (*3*) led to the identification of a new phase, with the composition $ZrO_2 \cdot 12Nb_2O_5$. The initial product of the reaction of the component oxides in these proportions is isostructural with $TiNb_{24}O_{62}$ (*4*, *5*), but on annealing, it transforms to a much more complex structure. Single crystal X-ray data from the transformed material indicated that the unit cell was probably monoclinic, with $a = c = 71.04$ Å, $b = 3.82$ Å, and $\beta \simeq 90°$. At the time that these observations were made (1964), a complete structure analysis was not considered, because of the magnitude of the problem of locating some hundreds of atoms in such a large unit cell.

The recent successful application of electron optical techniques to the large family of compounds which are structurally related to high temperature Nb_2O_5 (*6–8*) prompted us to re-open this investigation, and this paper describes the results of the current studies. The work provides a good example of the way in which electron diffraction and microscopy can, in favourable cases, considerably supplement the information obtained by X-ray methods.

2. Experimental

High purity ZrO_2 and Nb_2O_5 were mixed in the molar proportions 1:12 and heated in sealed platinum capsules at 1630–1640°K. The capsules were removed after 17 hr (Sample 1) and 161 hr (Sample 2) and quenched rapidly to room temperature.

Specimens for electron optical examination were prepared by techniques described previously (*6*). X-Ray powder diffraction patterns were recorded using a Guinier focussing camera, internally calibrated with KCl. Electron diffraction patterns were calibrated by depositing a thin layer of aluminium on to carbon-coated grids bearing the oxide samples.

3. Results

Three different components were found by electron diffraction in the two samples of $ZrO_2 \cdot 12Nb_2O_5$. These will be referred to as the α, β, and γ' components, and will be discussed in turn. An inspection of the electron diffraction patterns from a large number of fragments showed that about one third of Sample 1 was the α form, the remainder being β. None of the α form was found in Sample 2; the majority (ca. 90%) was β, and a few fragments of the γ' component were detected.

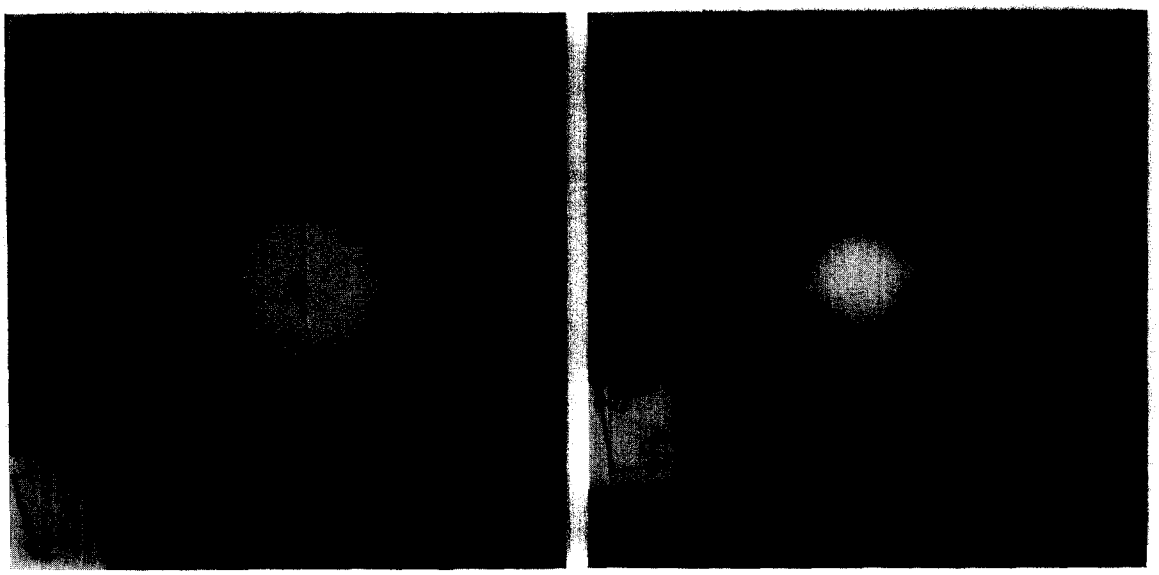

FIG. 1. Electron diffraction patterns from fragments of α-$ZrO_2 \cdot 12Nb_2O_5$. (a) *h0l* reciprocal lattice section. The square ReO_3-type subcell is outlined. (b) *hk*0 reciprocal lattice section, showing the absence of reflections for which $h + k \neq 2n$.

3.1. α-$ZrO_2 \cdot 12Nb_2O_5$

Electron diffraction patterns of the α form are shown in Fig. 1. The appearance of the *h0l* reciprocal lattice section (Fig. 1a) corresponds closely to that of $TiNb_{24}O_{62}$ (*7*), as do the unit cell dimensions derived from these patterns, viz,

$$\alpha\text{-}ZrO_2 \cdot 12Nb_2O_5$$

$$a = 29.5 \text{ Å}, b = 3.82 \text{ Å}, c = 21.1 \text{ Å}, \beta = 94.8°;$$

$$TiNb_{24}O_{62} \text{ (5)}$$

$$a = 29.78 \text{ Å}, b = 3.821 \text{ Å}, c = 21.12 \text{ Å}, \beta = 94.9°.$$

In the *hk*0 reciprocal lattice section of the α form (Fig. 1b), the allowed reflections are of the type $h + k = 2n$, indicating side-centred symmetry, which further confirms that this phase is isostructural with $TiNb_{24}O_{62}$.

Some of the *h0l* patterns showed streaking parallel to a^*, and lattice images from crystals tilted to reveal the shear planes parallel to *c* (e.g., Fig. 2) showed evidence for some disordered Wadsley intergrowth of the type found previously in the composition region between $TiNb_{24}O_{62}$ and Nb_2O_5 (*7*). Most of the fringes in Fig. 2 have a separation of 15 Å, which is the characteristic spacing between shear planes parallel to *c* in the $TiNb_{24}O_{62}$ structure, but there are a number of 17 Å separations, indicative of the intergrowth of planar slabs of the high temperature Nb_2O_5 structure. In the region marked *Z*, the 15 and 17 Å fringes alternate regularly, and by analogy with the TiO_2–Nb_2O_5 system (*7*), this may be regarded as a microdomain of the ordered intergrowth phase $ZrNb_{52}O_{132}$.

The concentration of Wadsley intergrowth defects varied considerably from one fragment to another, and the average concentration could easily be an order of magnitude less than is indicated by the example shown in Fig. 2. The consequent small departures from stoichiometry may possibly result from a very slight deficiency of ZrO_2 in the original preparation, or from the presence of minute amounts of another phase, higher in ZrO_2 content, in the sample.

3.2. β-$ZrO_2 \cdot 12Nb_2O_5$

The *h0l* diffraction pattern of the β component is shown in Fig. 3a. It is clearly very much more complex than that of the α form (Fig. 1a), and the unit cell dimensions derived from this and the *hk*0 and 0*kl* patterns (Fig. 3b, c) were

$$a = 39.7 \text{ Å}, b = 3.83 \text{ Å}, c = 35.8 \text{ Å}, \beta = 116.6°.$$

The presence of reflections for all possible values of *h*, *k*, and *l* in each of these patterns indicates primitive symmetry; this conclusion was confirmed by recording *h0l* and *h1l* X-ray data from a single crystal, using the Weissenberg method. All the lines in a Guinier X-ray powder pattern of Sample 2 were satisfactorily indexed on the basis of this unit cell.

Several lattice images, taken from the same area of a fragment of the β phase under different diffraction conditions, are reproduced in Fig. 4. In Fig. 4a,

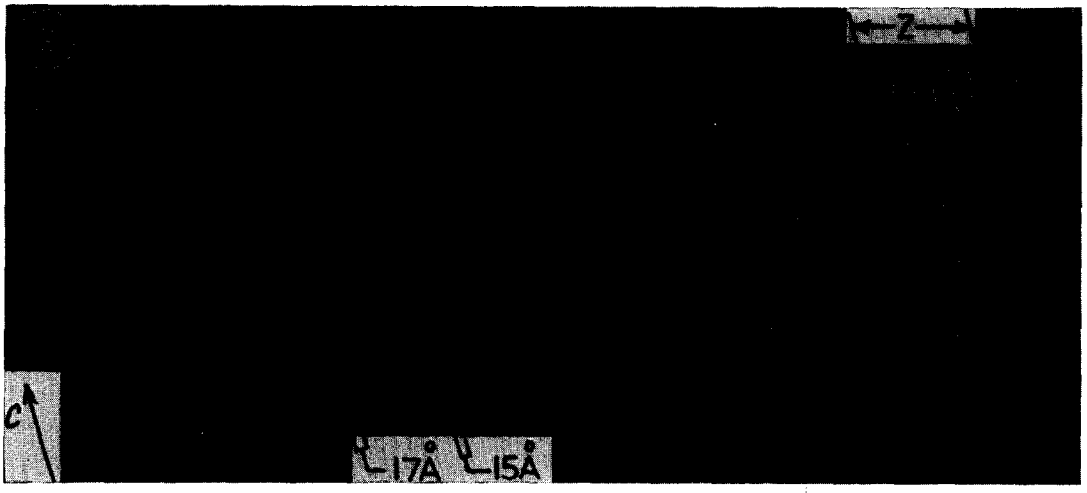

FIG. 2. Lattice image from a fragment of α-$ZrO_2 \cdot 12Nb_2O_5$, oriented so that only $h00$ reflections were contributing to the image. The black lines parallel to c are shear planes, and their spacings are either 15 Å, characteristic of the $TiNb_{24}O_{62}$ type structure, or 17 Å, characteristic of high temperature Nb_2O_5. The region Z is an ordered microdomain, with the probable composition $ZrNb_{52}O_{132}$.

the orientation of the fragment was such that the electron beam was incident exactly parallel to the short b axis. Under these conditions, the contrast in the image might be expected to provide some clue to the structure of the fragment (*8*). The main features of the micrograph are illustrated by the diagrammatic inset, and the unit cell of the repeating pattern is outlined. The contrast may be approximately described as an array of dots and streaks, arranged in lines parallel to c. Over most of the area, the lines contain alternately all dots, and a regular sequence of dots and streaks. This arrangement is interrupted along the fault labelled P, where two rows of dots are adjacent. Several more subtle disturbances labelled Q can be seen by viewing the image in the a direction. These faults are much more obvious in the image in Fig. 4b, which was recorded after tilting the fragment until the $00l$ reflections dominated the diffraction pattern.

3.3. γ'-$ZrO_2 \cdot 12Nb_2O_5$

Fragments of the γ' form gave diffraction patterns of the type shown in Fig. 3d. There is a strong similarity between this pattern and that of the β phase (Fig. 3a). Many of the reflections are common to both patterns, but in order to account for all the reflections in Fig. 3d, a large tetragonal unit cell, with $a = b \approx 71$ Å, and probably $c \approx 3.8$ Å, must be chosen. This unit cell corresponds closely to the one derived earlier by one of us (R.S.R.) from single crystal X-ray data (*3*). However, there are a large number of absent reflections in Fig. 3d, which are not of the type associated with absences due to space group symmetry. It seemed likely that the complexity of the pattern was due at least in part to twinning or some form of intergrowth, and this was confirmed by observing lattice images of the γ' form.

Figure 5a is a lattice image from a thin fragment, taken with the electron beam incident a few degrees away from parallelism with the short (3.8 Å) axis. The contrast in this case consists largely of an array of white dots, and it is immediately obvious that the area contains several distinct domains, each of which has a particular arrangement of these dots. In the area H, the dots are arranged in an approximately hexagonal pattern, but in S they lie in a square array, with a spacing of 35 Å. These patterns of dots can be readily reproduced on squared paper, and the crosses in Fig. 5b correspond to the white dots in the area enclosed by a rectangle in Fig. 5a. Measurements of the spacings of the dots indicate clearly that in the area H, they delineate unit cells of the β form of $ZrO_2 \cdot 12Nb_2O_5$. Therefore it appears that the γ' form is an intergrowth, containing domains of the β form and a second closely related tetragonal structure (area S) with the unit cell dimensions $a = 35.5$ Å, $c = 3.83$ Å, which we will refer to as γ-$ZrO_2 \cdot 12Nb_2O_5$. Two orientations of the β form are possible, having their a and c axes perpendicular to one another. Several narrow domains of the second orientation are labelled H_1 in Fig. 5a. The diffraction pattern in Fig. 3d can be synthesised by combining those of the two orientations of the β form (Fig. 3e, ii, iii), with the pattern

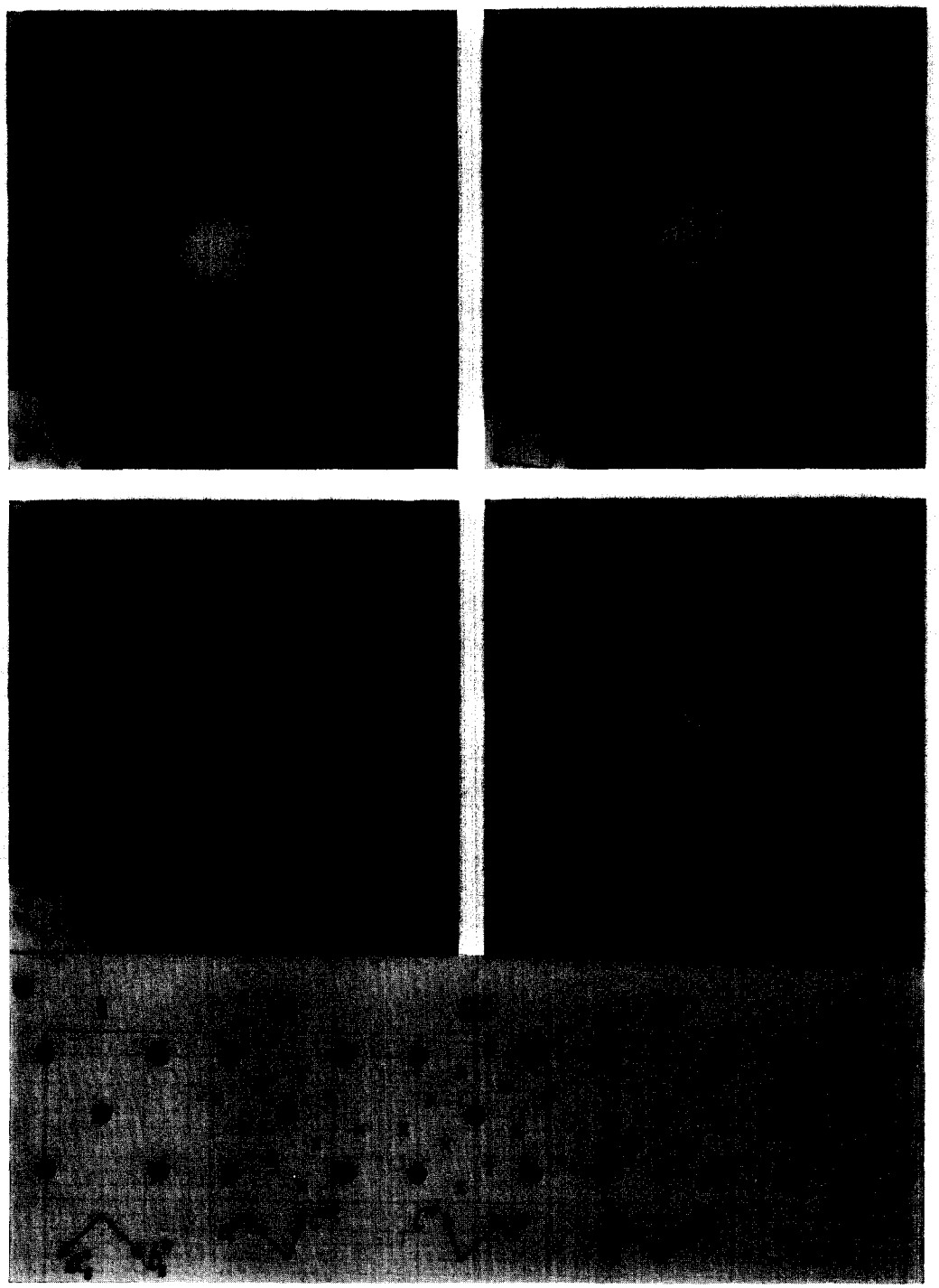

FIG. 3. Electron diffraction patterns from fragments of the β and γ' forms of $ZrO_2 \cdot 12Nb_2O_5$. (a) β form—*h0l* reciprocal lattice section; (b) β form—*0kl* reciprocal lattice section; (c) β form—*hk0* reciprocal lattice section; (d) γ' form—section corresponding to (a). (e) Relationship between the patterns of the β and γ' components. Each diagram is a representation of a small part of the pattern, corresponding to the square areas outlined in (a) and (d).

(i) Reflections from a tetragonal subcell, common to both patterns; (ii) Pattern of the β form; (iii) Pattern of the β form, oriented at right angles to (ii); (iv) Pattern expected from the γ form; (v) Composite of (ii), (iii), and (iv), corresponding to the pattern of the γ' form in (d).

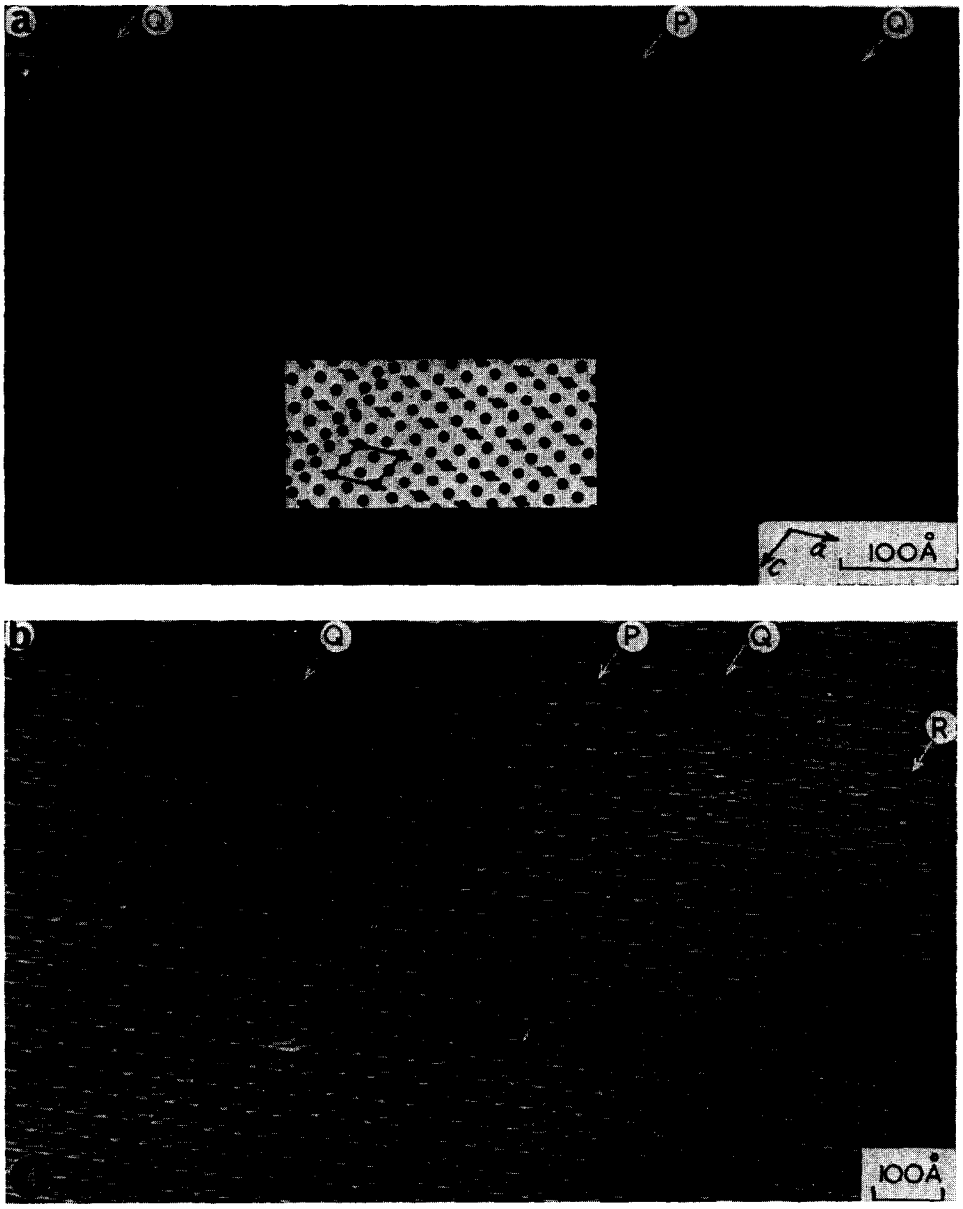

FIG. 4. Lattice images from a thin fragment of the β form of $ZrO_2 \cdot 12Nb_2O_5$, containing several faults, labelled *P*, *Q*, *R*. (a) Electron beam incident parallel to the short *b* axis. The inset depicts the main features of the contrast in an exaggerated way, and the unit cell of the β form is outlined. The fault *Q* can be observed by looking carefully along the *a* direction. (b) Image from the same area, slightly tilted from the orientation in (a), and at a lower magnification. The faults are now easily recognized.

expected from the γ form (Fig. 3e, iv). This process is illustrated diagrammatically in Fig. 3e, for the small section of the patterns outlined in Figs. 3a, d. Owing to the small size of the domains, it was not possible to verify this explanation of Fig. 3d directly by recording the electron diffraction patterns of the areas *S*, *H*, and H_1 separately.

4. Discussion

4.1. Possible Structures for β and γ-$ZrO_2 \cdot 12Nb_2O_5$

The diffraction patterns and lattice images presented here contain sufficient information to justify some discussion of possible idealized structures for these complex materials.

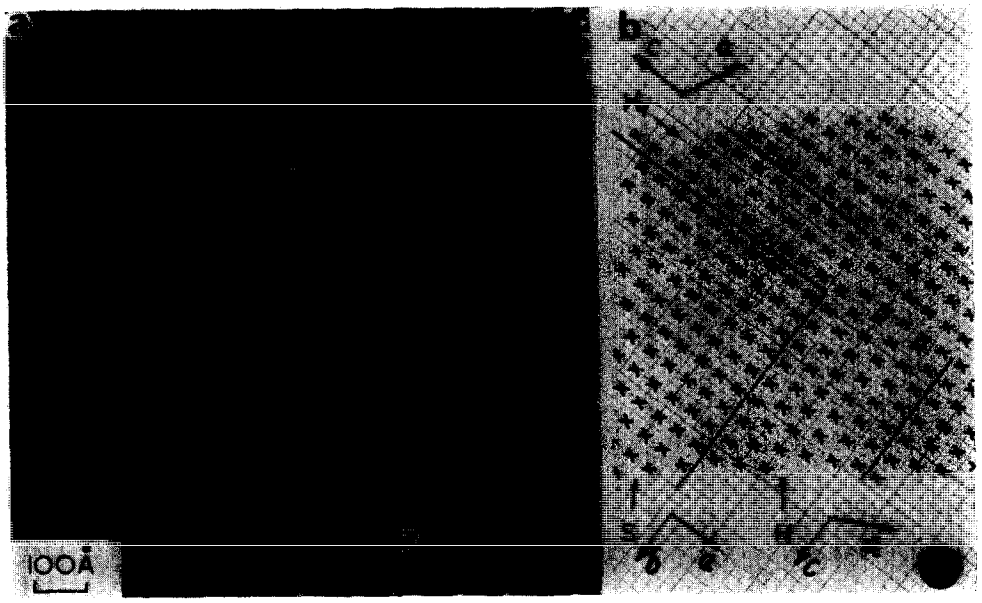

FIG. 5. (a) Lattice image from a fragment of γ'-$ZrO_2 \cdot 12Nb_2O_5$. The white dots delineate unit cells of the β form in the areas H and H_1, and of the γ form in the area S. (b) Representation of the enclosed area in (a), drawn on squared paper.

It has been amply demonstrated [e.g., Ref. (*6*)] that amongst the family of oxides based on the simple ReO_3 structure, and modified by the presence of two intersecting sets of crystallographic shear planes, the unit cell dimensions calculated from idealized models agree with observed values to within $\pm 2\%$, assuming a constant octahedral edge length of 2.89 Å. In addition to this criterion, any proposed model must have the correct symmetry and stoichiometry, and should also account, in a qualitative way, for the appearance of lattice images, particularly those in which the electron beam is incident parallel to the short axis (*8*). Finally, the defects which are observed in lattice images should also be capable of being accommodated in the model by means of relatively minor rearrangements of the component blocks of the idealized structure. These five requirements, which when taken together restrict the number of possible structures very substantially, provide a useful basis for deriving models.

An outstanding feature of the electron diffraction patterns in Fig. 3a, b and also in Fig. 1a, is the distribution of strong reflections in a square array (outlined in Fig. 1a) corresponding to a unit cell of about 3.8×3.8 Å in projection. This is typical of the high temperature Nb_2O_5 family of compounds (*9*), and is caused by the presence of blocks of corner-shared octahedra, which each have the cubic ReO_3 structure, with $a \approx 3.8$ Å. These blocks are joined to one another in the shear planes by sharing octahedral edges rather than corners, and the variable parameters which give rise to the different compositions and structures in the family are the sizes of the blocks and the detailed way in which they are joined together. For example, the idealized structure of $TiNb_{24}O_{62}$ (or α-$ZrO_2 \cdot 12Nb_2O_5$) is shown in Fig. 6a. In this case, the blocks are all 4 octahedra long by 3 wide, and the sides of adjacent blocks are joined by sharing octahedral edges. The regions at the corners of the blocks may be occupied by metal atoms in tetrahedral coordination (labelled *O* in Fig. 6a), or alternatively, four blocks may be joined at their common corner by sharing octahedral edges (labelled *X* in Fig. 6a).

It is clear from an inspection of the diffraction patterns in Fig. 3, that the β and γ forms of $ZrO_2 \cdot 12Nb_2O_5$ share a common tetragonal subcell, part of whose diffraction pattern is drawn in Fig. 3e, i. The dimensions of this subcell are: $a_s = 17.7$ Å, $c_s = 3.83$ Å. It seemed reasonable to suppose that the monoclinic and tetragonal lattices of the β and γ forms are derived from this subcell by some relatively minor rearrangement of structural components. Two models, shown in Fig. 6b,c, were derived for the subcell. They are both tetragonal, with calculated unit cell dimensions $a_s = 17.6$ Å, $c_s = 3.8$ Å, and they both have the correct stoichiometry, $M_{25}O_{62}$. In Fig. 6b, the blocks are all 4×3 in size, but unlike the structue in Fig. 6a, the blocks

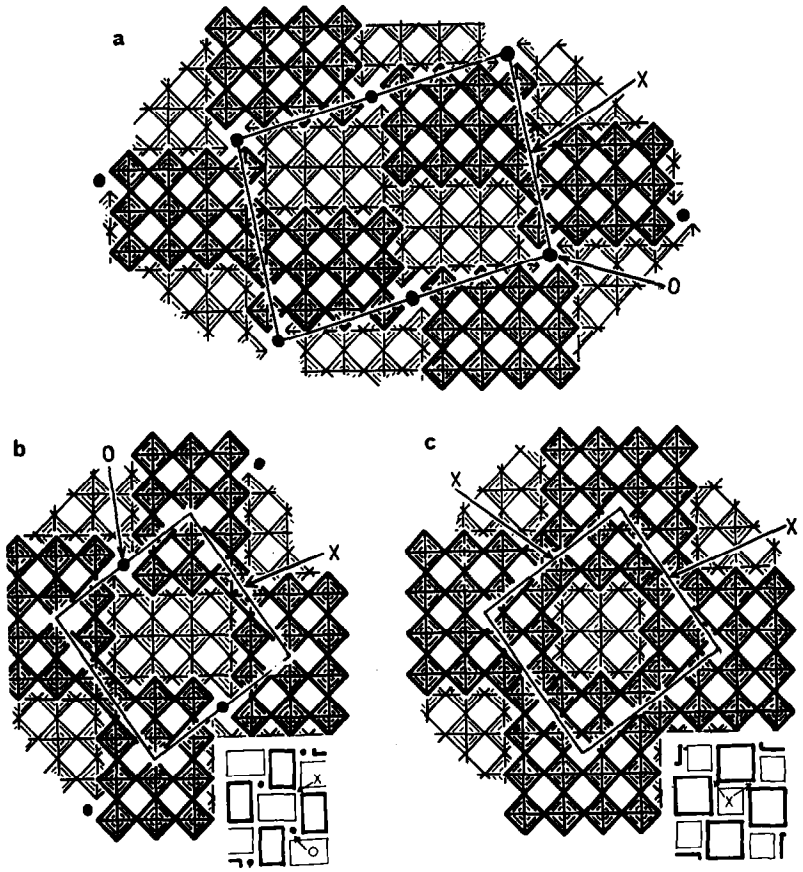

FIG. 6. Cross sections normal to the short (3.8 Å) axis of idealized structures of (a) $TiNb_{24}O_{62}$ (or α-$ZrO_2 \cdot 12Nb_2O_5$); (b) and (c) possible tetragonal subcells of β- and γ-$ZrO_2 \cdot 12Nb_2O_5$. Each square represents an octahedron viewed down a body diagonal, the lighter and darker squares being centred on two parallel planes 1.9 Å apart. The octahedra sharing corners form the structural blocks, and the junctions between light and dark are the shear planes where octahedra share edges. The circles (*O* positions) are atoms in tetrahedral coordination. At the *X* positions, neighbouring octahedra at the same level share edges. A simpler representation, in which each block of octahedra is drawn as a rectangle or square, is shown at the lower right of (b) and (c).

at the two levels (lighter and darker) are oriented at right angles to one another. The positions labelled *O* and *X*, at the corners of the blocks, are similar to those in Fig. 6a. In Fig. 6c, the blocks at one level are all 4×4 in size, and those at the other are all 3×3. In this case, the corners of all blocks are joined by sharing octahedral edges (*X* positions) and there are no atoms in tetrahedral coordination (*O* positions).

The geometrical relationship between the subcell and the unit cells of the β and γ forms of $ZrO_2 \cdot 12Nb_2O_5$ is readily derived from the diffraction patterns, and is shown in real space in Fig. 7. The calculated dimensions of the superlattices are as follows:

β-$ZrO_2 \cdot 12Nb_2O_5$ $\quad a = a_s \times \sqrt{5} = 39.4$ Å,
$\quad b = c_s = 3.8$ Å,
$\quad c = a_s \times 2 = 35.2$ Å.
$\quad \beta = 180° - \arctan(2) = 116.57°$

γ-$ZrO_2 \cdot 12Nb_2O_5$ $\quad a = a_s \times 2 = 35.2$ Å,
$\quad c = c_s = 3.8$ Å.

These values correspond closely with the experimental data obtained from the electron diffraction patterns, quoted earlier.

The lattice image in Fig. 4a, taken with the electron beam incident parallel to the *b* axis of the β form, provides useful information concerning the arrangement of structural components in the superlattice of this polymorph. It has been shown previously (*8*) that the sites occupied by tetrahedral atoms (*O* positions) in structures of this type produce strong contrast in the form of dark dots in

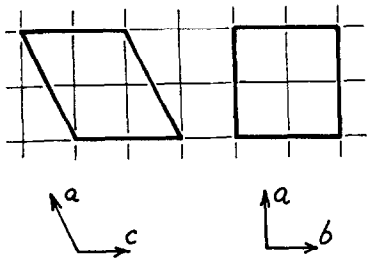

FIG. 7. Relationship between the unit cells of the β (left) and γ (right) forms of $ZrO_2 \cdot 12Nb_2O_5$, and the tetragonal subcell, which has the dimensions of the square grid. All the cells share a common short axis of 3.8 Å, perpendicular to the plane of the paper.

lattice images of fragments in this orientation. It seems likely therefore, that the dark dots in Fig. 4a, which are the major component of the observed contrast, can be correlated directly with *O* positions. This implies that the basic structure is more likely to be that shown in Fig. 6b than that in Fig. 6c, because the latter does not contain *O* positions. An extended area of this structure is drawn schematically in Fig. 8a, and a comparison of the arrangement of *O* positions in this model and that of the dark dots in Fig. 4a indicates that there is good correspondence except in the regions marked by circles, where the lattice image contrast is a streak rather than a dot. A fault labelled *P* is included in the model, and the distribution of *O* positions in this region correlates well with the contrast in the vicinity of the fault *P* in Fig. 4a.

A large proportion of the contrast is therefore accounted for on the basis of the subcell in Fig. 6b, but some modification of this structure in the encircled regions of Fig. 8a is required in order to increase the size of the unit cell, and account for the streak contrast in the corresponding positions in the lattice image. The most obvious way of achieving this modification is to "mix" the subcell in Fig. 6b with that in Fig. 6c in an appropriate way, and produce an intergrowth structure. This process is illustrated in Fig. 8b. A small number of the 4×3 blocks have been replaced by 4×4 and 3×3

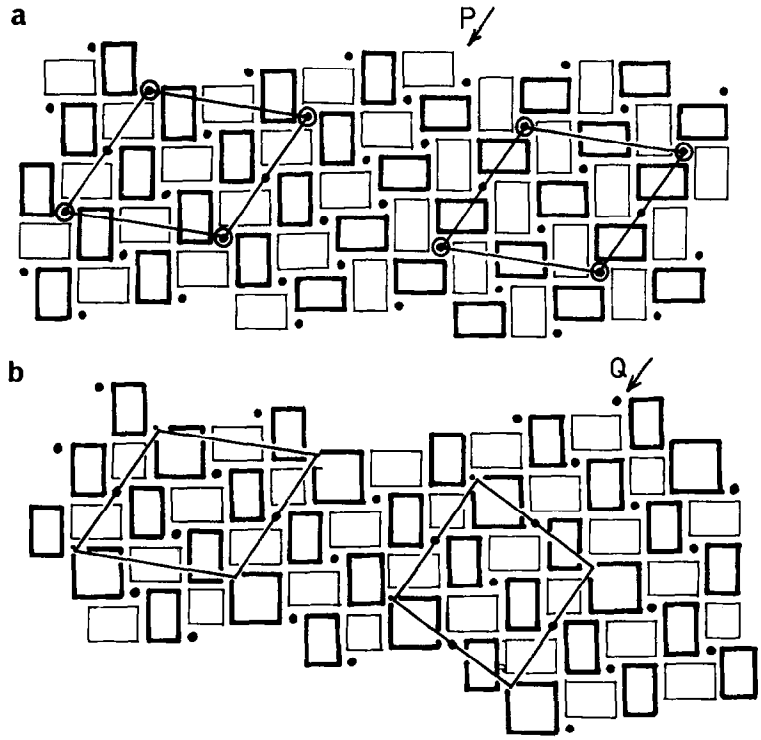

FIG. 8. (a) Extended area of the structure shown in Fig. 6b, modified in the region marked *P* in order to explain the appearance of the fault *P* in Fig. 4a. Unit cells of the β form of $ZrO_2 \cdot 12Nb_2O_5$ are outlined, and the circles indicate the areas of the subcell structure which require modification in order to explain the observed unit cell size, and the contrast in Fig. 4a.

(b) Extended area of the structure shown in Fig. 6b, modified periodically by "mixing" into it, areas of the structure shown in Fig. 6c. Unit cells of the β (left) and γ (centre) forms are outlined. The model corresponds to the insertion of a slab of the γ form, one unit cell wide, in a matrix of the β form, similar to the faults labelled *Q* in Fig. 4.

blocks, with the consequent conversion of some of the *O* positions to *X* positions. There are a variety of ways in which the "converted *O* positions" can be arranged, to give unit cells corresponding to the monoclinic β form (Fig. 8b, left) or the tetragonal γ form (Fig. 8b, centre). The area modelled in Fig. 8b corresponds to the area around the fault *Q* in Fig. 4a. This implies that the fault *Q* is in fact a slab of the γ form, one unit cell wide, intergrown with the β form. Both unit cells have the same volume, and each contains four subcell units, and a total of 100 metal atoms and 248 oxygen atoms, equivalent to 4 "molecules" of $ZrNb_{24}O_{62}$. The unit cells are primitive and non-centric, and the proposed structure of the γ form does not possess the fourfold axis required for true tetragonal symmetry. Hence it must be regarded as monoclinic, with the same space group as the β form, namely *Pm*.

While the proposed structures account very well for the majority of the diffraction and lattice image data, they do not satisfactorily explain the streak contrast in the lattice image of Fig. 4a. The regions which give this contrast are correlated in Fig. 8b with *X* positions, created by modifying the subcell structure in Fig. 8a periodically. However, previous studies (*8*, *10*) have indicated that similar *X* positions give much less contrast than *O* positions, while in Fig. 4a, the streaks and dots appear to be of similar intensity. Secondly, there are a number of other *X* positions in the structures, and it is obvious that if they all produced the same streak contrast, the images would appear quite different. These criticisms of the proposed structures are based on a rather limited amount of experience, and it must be remembered that the appearance of lattice images is critically dependent on several factors which are not easily specified. In particular, the contrast in lattice images is strongly influenced by the thickness of the crystal fragment, and by the position of focus of the electron beam with respect to the exit face of the fragment (*11*). We therefore do not feel justified in rejecting the models on the basis of a single micrograph. We have been unable to derive an alternative model which has the correct composition and is consistent with all the observed data.

4.2. Defects in the β and γ Polymorphs

The defects evident in the lattice images in Figs. 4 and 5 can all be satisfactorily accounted for in terms of the proposed models. The inset to Fig. 4a was prepared by making a model of the area including the defects labelled *P* and *Q* (parts of which appear in Fig. 8) and reproducing only the *O* positions (dots) and "converted *O* positions" (streaked dots) on the same scale as the micrograph. Similar models can also be proposed to account for the arrangement of white dots in Fig. 5a, if it is assumed that each white dot corresponds to a "converted *O* position." This micrograph shows that very pronounced changes of contrast may accompany a change of orientation of a few degrees from the condition for images such as Fig. 4a, in which the electron beam is incident parallel to the short axis of the structure.

Most of the defects can be adequately described in terms of the intergrowth of slabs of the γ form in a matrix of the β form or vice versa. Those labelled *Q* in Fig. 4 are one unit cell wide, and may be regarded as antiphase boundaries, because they cause a displacement of the β matrix of half a unit cell in the *c* direction. This is clearly seen by observing the shift of the dark fringes in Fig. 4b, as they traverse the defects. The fault *R* in Fig. 4b is probably a slab of the γ form two unit cells wide, because in this case, the dark fringes are displayed by a complete unit cell.

Because the β and γ forms have the same composition, none of these defects alter the stoichiometry of the fragments. However, the fault labelled *P* in Fig. 4 is of a different character. The displacement in the *c* direction is about one-quarter of a unit cell (Fig. 4b), and the model in Fig. 8a indicates that it also causes a displacement of half a unit cell in the short *b* direction. The orientation of the 4×3 blocks at each level, represented by dark and light lines in Fig. 8a, is reversed on either side of the fault. The arrangement of blocks and *O* positions along the fault is identical to that found in the related phase $WNb_{12}O_{33}$ (*12*), and the fault may therefore be regarded as a slab of the $M_{13}O_{33}$ structure, half a unit cell wide. Thus in this case, the presence of the fault alters the stoichiometry of the crystal, in the direction of an increased oxygen–metal ratio, i.e., towards Nb_2O_5. This is consistent with the observation that Wadsley intergrowth defects which were found in the α polymorph (Section 3.1) also indicated a small departure from the stoichiometry $ZrNb_{24}O_{62}$, in the direction of Nb_2O_5.

4.3. Further Work

The intention of the present work was to investigate the polymorphism of $ZrO_2 \cdot 12Nb_2O_5$. The occurrence of the phenomenon was clearly indicated by X-ray studies, but very little detailed information was derived. By applying electron optical techniques, we have successfully identified three polymorphs, determined the unit cell dimensions of each, and

observed intergrowth defects and microdomains in individual fragments. We have also proposed idealized models for the structures of the β and γ forms. The validity of these models will be tested by a complete X-ray structure analysis of the β form, which is to be carried out by Dr. N. C. Stephenson, at the University of New South Wales, Australia. It is expected that the idealized model (Fig. 8b, left) should serve as a useful trial structure, and at least provide a basis for the interpretation of the Patterson function.

The observations discussed in this paper were made on two samples, which differed only in their heat treatments, and it is clear that the system ZrO_2–Nb_2O_5 warrants further investigation. We propose to examine a series of compositions in this system in order to make a more careful comparison with the TiO_2–Nb_2O_5 system (*1*, *7*), and also to discover how the polymorphism is affected by changes in stoichiometry. The stability relations of the various forms of $ZrO_2 \cdot 12Nb_2O_5$ may also be elucidated by carrying out additional annealing treatments. The present experimental evidence is not sufficient to determine whether the β and γ phases actually have polymorphic stability ranges, or are truly polytypic.

4.4. Comparison of X-ray and Electron Optical Techniques

The present work provides a good example of the way in which electron optical techniques can be used to advantage in conjunction with X-ray diffraction procedures in studies of complex structures. It is important to recognize that in the present instance, the structures all belong to a family, and that the building principles which apply to all the members of the family were firmly established initially by the application of conventional single crystal X-ray methods. In particular, the determination of the structure of high temperature Nb_2O_5 (*13*) provided the insight which led to the identification of a very large number of closely related oxides and oxide fluorides of complex but specific stoichiometry (*9*). Without this accumulation of X-ray data, the interpretation of the electron optical observations, which have now been made on many members of the family, would have been highly speculative, if not impossible.

The major differences between electron diffraction and X-ray diffraction follow directly from a comparison of two important properties:

(i) The wavelength of 100-kV electrons is 0.037 Å, of the order of one fiftieth of that of X-rays. The effects of this difference are that the Bragg angles are all much smaller than for X-rays, and that the Ewald sphere is nearly a plane section through the reciprocal lattice (*14*). For this reason, it is possible to record quite extensive sections of the reciprocal lattice directly. Thus the diffraction patterns shown in Figs. 1 and 3 correspond closely to zero layer patterns obtained by the X-ray precession technique, but in the case of electrons the crystal fragments remain stationary while the patterns are recorded.

(ii) Scattering factors for electrons are about three orders of magnitude greater than for X-rays. For this reason, it is necessary to use very thin specimens for transmission electron diffraction, and, coupled with the facility of selecting very small areas from the field of view in the microscope, it is possible to obtain diffraction patterns from "single crystals" which may be only 10^{-9} cm^2 in area and about 10^{-6} cm thick. Secondly, since a high proportion of the incident beam suffers diffraction, the diffraction pattern can be viewed directly on a fluorescent screen, and recorded on a photographic plate in a few seconds, compared with many hours for an X-ray pattern. For example, *h0l* X-ray data were collected from a single crystal needle of β-$ZrO_2 \cdot 12Nb_2O_5$ by the Weissenberg method, and during an exposure of 70 hr, only about 25% of the possible reflections were recorded. Thus in this case, the unit cell dimensions and symmetry were much more easily derived from electron diffraction data such as that shown in Fig. 3.

The large scattering factors for electrons also have less favourable consequences. In most circumstances, the diffracted beams are strongly influenced by dynamical effects such as multiple reflection and inelastic scattering, and their intensities cannot normally be used directly as data for structure analysis (*14*). Nevertheless, it is clear from the present work that provided very thin fragments are selected for diffraction, the intensities have considerable qualitative significance, and we have made use of the appearance of the diffraction patterns to draw conclusions as to the nature of the basic structure; in this case the ReO_3 structure.

A second unfortunate consequence of the strong interaction of the incident electrons with the specimen is that reflections which are formally forbidden by space group extinction rules may be excited with appreciable intensity (*14*). Therefore considerable care must be exercised when deriving symmetry data from electron diffraction patterns. The most straightforward way of minimizing these complica-

tions is to work with very thin fragments, and thereby reduce dynamical effects to a minimum.

Perhaps the most important advantage of electron optical techniques is the facility with which transmission observations at high magnification can be made. The ability to record images and diffraction patterns from the same area of a sample at a number of different orientations has been exploited very extensively and successfully by physicists and metallurgists for the study of defects in metals and alloys. These methods are equally applicable to nonmetallic materials, and are certain to find increasing use in solid state chemistry. Recent studies of TiO (*15*) and slightly reduced TiO_2 (*16*) illustrate some of the applications in this field.

The possibility of obtaining structural information directly from high resolution lattice images of crystals has not yet been explored in detail. Until quite recently, lattice images were regarded mainly as a means of checking magnification and resolution in the electron microscope, but it is clear from our present studies of complex oxides that in favourable cases, they may contain a wealth of potentially useful information. For example, we have been able to use the appearance of domains in a lattice image (Fig. 5a), to explain the arrangement of reflections in a complex electron diffraction pattern (Fig. 3d). We have also made direct correlations between image contrast (Fig. 4a) and specific features in proposed model structures (Fig. 8). These correlations were based on more extensive observations on known structures (*7*, *8*), and the theoretical implications of this work are currently being investigated (*11*). The contrast in lattice images is also influenced by dynamical effects in the same way as electron diffraction patterns, and their appearance is also dependent on the orientation of the sample and the focussing conditions. In spite of these complicating factors, there is good reason to expect that these methods will be successfully applied to many solid state problems in the future.

Note added in proof: The subcell structure in Fig. 6b is orthorhombic, not tetragonal as described in the text, because it does not possess a fourfold axis of symmetry.

Acknowledgments

We wish to thank Dr. W. G. Mumme and Dr. B. M. Gatehouse for their assistance with the single-crystal measurements, and Dr. J. V. Sanders for his continued interest and valuable criticism.

References

1. R. S. Roth and L. W. Coughanour, *J. Res. Nat. Bur. Stand.* **55**, 209 (1955).
2. H. J. Goldschmidt, *Metallurgia* **62**, 217 (1960).
3. R. S. Roth, unpublished results.
4. J. L. Waring and R. S. Roth, *J. Res. Nat. Bur. Stand. Sect. A* **69**, 119 (1965).
5. R. S. Roth and A. D. Wadsley, *Acta Crystallogr.* **18**, 724 (1965).
6. J. G. Allpress, J. V. Sanders, and A. D. Wadsley, *Acta Crystallogr. Sect. B* **25**, 1156 (1969).
7. J. G. Allpress, *J. Solid State Chem.* **1**, 66 (1969).
8. J. G. Allpress, *Mater. Res. Bull.* **4**, 707 (1969).
9. A. D. Wadsley and S. Andersson, *in* "Perspectives in Structural Chemistry," (J. D. Dunitz and J. A. Ibers, Eds.), Vol. III, John Wiley and Sons, Inc., New York, 1970, in press.
10. J. G. Allpress, *J. Solid State Chem.* **2**, 78 (1970).
11. E. Chidzey, unpublished results.
12. R. S. Roth and A. D. Wadsley, *Acta Crystallogr.* **19**, 32, (1965).
13. B. M. Gatehouse and A. D. Wadsley, *Acta Crystallogr.* **17**, 1545 (1964).
14. See, e.g., J. M. Cowley, *in* "Progress in Materials Science," (B. Chalmers and W. Hume-Rothery, Eds.), Vol. **13**, No. 6, Pergamon Press, Oxford, 1967.
15. D. Watanabe, J. R. Castles, A. Jostsons, and A. S. Malin, *Acta Crystallogr.* **23**, 307 (1967).
16. L. A. Bursill, B. G. Hyde, O. Terasaki, and D. Watanabe, *Phil. Mag.* **20**, 347 (1969).